

## Article

# Prospects of Geoinformatics in Analyzing Spatial Heterogeneities of Microstructural Properties of a Tectonic Fault

Stepan Ustinov <sup>1,2,\*</sup>, Alexey Ostapchuk <sup>2,3,\*</sup>, Alexey Svecherevskiy <sup>1</sup>, Alexey Usachev <sup>2,3</sup>, Grigorii Gridin <sup>2</sup>, Antonina Grigor'eva <sup>1,2</sup> and Igor Nafigin <sup>1</sup>

<sup>1</sup> Institute of Geology of Ore Deposits, Petrography, Mineralogy and Geochemistry of the Russian Academy of Sciences, 119017 Moscow, Russia; svecherevskiy@igem.ru (A.S.); grig@igem.ru (A.G.); nafigin@igem.ru (I.N.)

<sup>2</sup> Sadovsky Institute for Dynamics of Geospheres of the Russian Academy of Sciences, 119334 Moscow, Russia; usachev.ad@phystech.edu (A.U.); gridin.grigorii@phystech.edu (G.G.)

<sup>3</sup> Moscow Institute of Physics and Technology, 141701 Dolgoprudny, Russia

\* Correspondence: ustinov@igem.ru (S.U.); ostapchuk.aa@phystech.edu (A.O.)

**Abstract:** The paper proposes a special technique for microstructural analysis (STMA) of rock samples based on two provisions. The first one is an algorithm for the automatic detection and digitalization of microstructures in images of oriented thin sections. The second one utilizes geographic information system (GIS) tools for an automatized analysis of objects at the micro scale. Using STMA allows the establishment of geometric features of fissure and pore space of rock samples to determine the parameters of stress–strain fields at different stages of rock massif deformation and to establish a relationship between microstructures and macrostructures. STMA makes it possible to evaluate the spatial heterogeneity of physical and structural properties of rocks at the micro scale. Verification of STMA was carried out using 15 rock samples collected across the core of the Primorsky Fault of the Baikal Rift Zone. Petrographic data were compared to the quantitative parameters of microfracture networks. The damage zone of the Primorsky Fault includes three clusters characterized by different porosity, permeability, and deformation type. Findings point to the efficiency of STMA in revealing the spatial heterogeneity of a tectonic fault.

**Keywords:** microstructural analysis; GIS technology; image analysis; image filtering; microfracture mapping; porosity; permeability; Primorsky Fault; tectonite; Baikal Rift Zone



**Citation:** Ustinov, S.; Ostapchuk, A.; Svecherevskiy, A.; Usachev, A.; Gridin, G.; Grigor'eva, A.; Nafigin, I. Prospects of Geoinformatics in Analyzing Spatial Heterogeneities of Microstructural Properties of a Tectonic Fault. *Appl. Sci.* **2022**, *12*, 2864. <https://doi.org/10.3390/app12062864>

Academic Editors: Alexei Gvishiani and Boris Dzeboev

Received: 29 January 2022

Accepted: 8 March 2022

Published: 10 March 2022

**Publisher's Note:** MDPI stays neutral with regard to jurisdictional claims in published maps and institutional affiliations.



**Copyright:** © 2022 by the authors. Licensee MDPI, Basel, Switzerland. This article is an open access article distributed under the terms and conditions of the Creative Commons Attribution (CC BY) license (<https://creativecommons.org/licenses/by/4.0/>).

## 1. Introduction

One of the main tasks of tectonophysics and structural geology is to establish the hierarchical rank of tectonic stress fields from local [1–3] and subregional [4,5] to regional [6–8] and global [9–12] ones. Depending on the tasks being solved and the scale of the objects under study, various methods from microstructural and petrophysical analyses to numerical methods of continuum mechanics and physical modeling are used [13–15]. A reconstruction of the stress–strain field can be successful only after detailed structural studies, mapping smallest changes in tectonic deformations and taking into account the lithological factors and the interaction of structures at different scales [16,17]. Additional information in many cases can decide the interpretation of the obtained data. For example, a comprehensive study of the mechanical, hydraulic and seismological properties of a fault allows the consideration of various components of the fault structure and permits the creation of a most accurate model of the fault [18–20]. Actually, the structure of a fault zone being determined provides information forecasting its mechanical behavior [19]. Determining orientation and distribution of microfractures along a large fault helps in verifying the tectonophysical data obtained in macrofracture measurements [21]. Additionally, studying microfractures in oriented rock samples may be used to define paleostress conditions in the rock at the time when the microfractures formed [22–24].

Microstructural analysis in geology is mainly used to establish the spatial and temporal relationship between microfracture ensembles of different genetic types, as well as to reconstruct the stress–strain fields, which act within small volumes of mineral aggregates [25–28]. The technique of traditional microstructural analysis is reduced to statistical measurements of the position of certain crystallographic or optical elements of grains of some minerals in the rock. Resting on the typification of orientations for a single mineral and different minerals in polymineral formations observed in stereograms, S-, B- and R-tectonites are identified. For S-tectonites the optical axes and other crystallographic elements of mineral grains are directed in different ways. This is expressed in one or two maxima in stereograms. B-tectonites in stereograms are characterized by a series of maxima located within a certain belt, the axis of which is perpendicular to the deformation plane. Sometimes, rocks are characterized by an orientation with a relatively uniform belt density of R-tectonite type [29]. One accumulated an extensive database on spatial orientations of various minerals, textural and structural features of rocks of various genesis and composition. However, the main problem of the traditional microstructural analysis method is the technical complexity of its implementation, which implies the use of a four-axis Fedorov stage mounted on a microscope, the lack of a computer automated software, the need to obtain a large amount of data and the extremely ambiguous interpretation of the data [10]. Measurements of crystallographic and optical elements of mineral grains in this case have to be carried out manually, which takes a lot of time.

Cracks and microcracks form mainly in the zone of brittle deformations as a response to the external stress [9,30–33]. Tectonic stresses result in the formation of permeable fractures or cause shear disturbances in pre-existing open fractures [34]. In the shallow crust the brittle deformation is predominant, and the intensity of deformation increases with depth and is relatively independent on temperature, rock type and strain rate [2]. Brittle deformation significantly depends on the coefficient of friction, the pressure of pore fluids and the orientation of the structure relative to the axes of the stress–strain field [33,34]. In contrast, at deep crust, ductile deformation is predominant and is highly dependent on temperature, strain rate and rock type [35]. The temperature increase results in a brittle–ductile transition, and rocks are characterized by brittle properties at low temperatures and acquire ductile characteristics at high temperatures (hundreds of degrees). The brittle–ductile transition usually takes place in the temperature range of 370–400 °C [36,37].

Porosity and permeability determine physical properties of the rock and characterize the fissure-pore space available for the pathway of fluids and deposition of minerals [38]. Porosity and permeability are directly related to the structural properties of the rock and can be calculated using geometric analysis of fractures [38,39]. Geometric analysis includes the determination of mean fracture orientation, length, aperture and volumetric density [40–50]. Fracture network parameters can be estimated manually by using semi-automatic and automatic measurements in rock samples [51–54] and indirectly by using electrical conductivity,  $V_p$  and  $V_s$  velocity measurements [38]. Other approaches, involving techniques such as X-ray tomography [55,56] or confocal scanning laser microscopy (CSLM) [57] are also used.

Methods of microstructural analysis always rest on the determination of geometric parameters of all microfractures, for which its number can reach hundreds of thousands in a single-oriented thin section. Obviously, without using any special technique of automatic detection, the solution of this problem is not only technically complex but is also time consuming. Many works present results of successful automatic lineament detection at microscales [27,58–60], mesoscales [61,62] and macroscales [61–63]. The development of digital technologies allows taking a fresh look at microstructural analyses.

The geospatial binding of thin sections allows the performance of microfracture detection by mapping objects at the area of thin section, which can be a conditional cartographic basis. GIS techniques can be used to solve spatial problems. In terms of territorial coverage, it is customary to distinguish between global GIS, subcontinental GIS, national GIS, regional GIS, subregional GIS and local GIS [64–66]. Geospatial binding of thin sections allows the performance of the transition from macro-GIS projects to micro-GIS.

This paper presents a new approach for the microstructural analysis of rock samples based on an algorithm of automatically mapping microfractures and their geospatial binding using GIS tools. The advantages of STMA method are shown by analyzing the microfractures of rock samples collected across the core of the Primorsky Fault. In the context of ongoing microstructural studies, given that the studied rock samples belong directly to the damage zone of the Primorsky Fault, the rocks were characterized by the type of tectonites among other parameters. In most cases, tectonites are defined as rocks that have experienced tectonic stress [67,68]. Rocks with pronounced schistosity are presented by protomylonites, blastomylonites, mylonites and ultramylonites. Rock samples without obvious schistosity are subdivided into protocataclasites, blastocataclasites, cataclasites and ultracataclasites. Mylonites are fine-grained, siliceous, very densely banded or vein-like rocks resulting from the fine crushing of coarse-grained rocks without noticeable chemical transformations. Mylonites are the end product of intensive dislocation metamorphism [67,68]. Cataclasites are rocks that formed during discontinuous deformations (brecciation and crushing) of brittle parent rocks. Cataclasites gradually transform into mylonites via a decrease in grain size and the development of banded textures.

## 2. Materials and Methods

The research methodology is aimed at identifying the heterogeneity of the fault zone based on the analysis of the spatial distribution of microfracture parameters. The main emphasis is conducted on a detailed description of the developed automatic identification and mapping of microfractures. Figure 1 shows a flowchart of the research protocol.

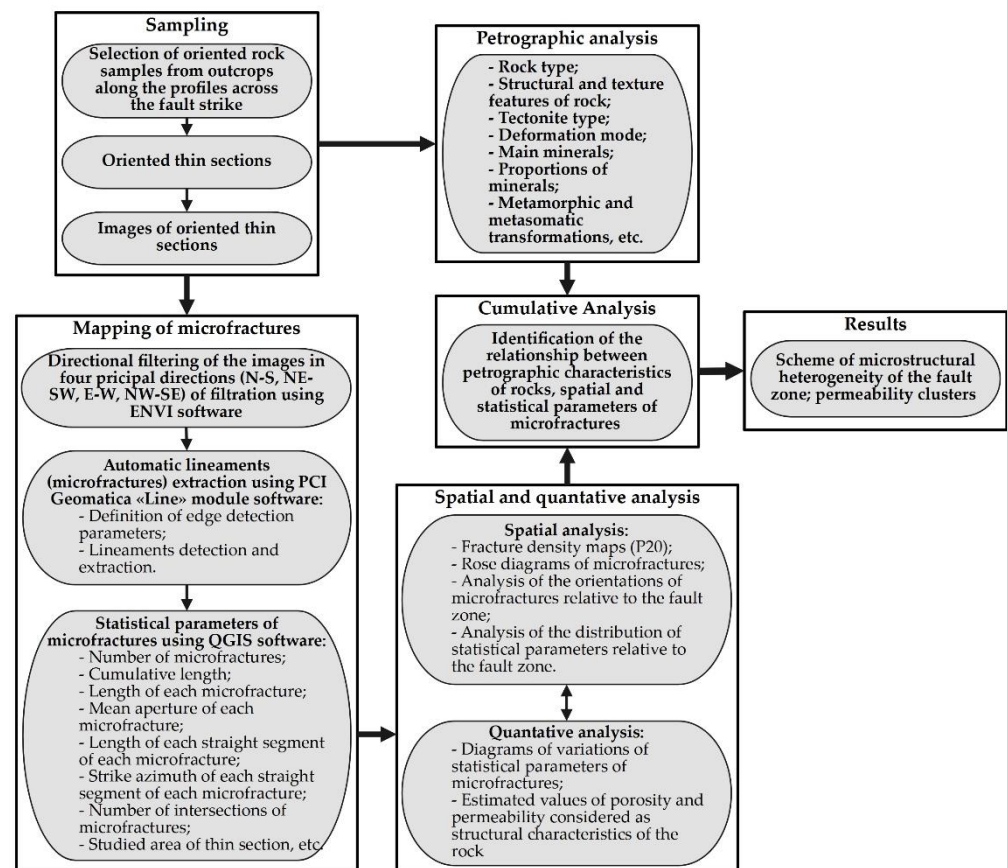


**Figure 1.** Flowchart of the research protocol.

### 2.1. Area of Study

Oriented rock samples were taken from outcrops across the strike of the Primorsky deep fault of the Baikal Rift Zone (Irkutsk region, Russia) in the area of the Sarma river

(Figure 2). The Primorsky Fault is the largest and best-documented neotectonic structure [69–75] in the region. It belongs to the Obruchev fault system [76,77].

The main thrust event occurred in the Paleozoic [78], but the compression structures became active again in later tectonic events. The age of the last activity remains poorly established and varies from Mesozoic to Miocene–Pliocene in different models [78–81]. The setting of neotectonic regional stress changed from early orogenic shear strike-slip about 30 million years ago to late orogenic extension about 3 million years ago [80]. The faults of the Obruchev system, which stretch for hundreds of kilometers in the northeasterly direction, have experienced different stages of evolution and can be studied via field structural measurements. The main trace of the Primorsky Fault, which was formed at the final phase of the collapse, is geomorphologically expressed as a ledge and is available for geological surveys for over more than 200 km.

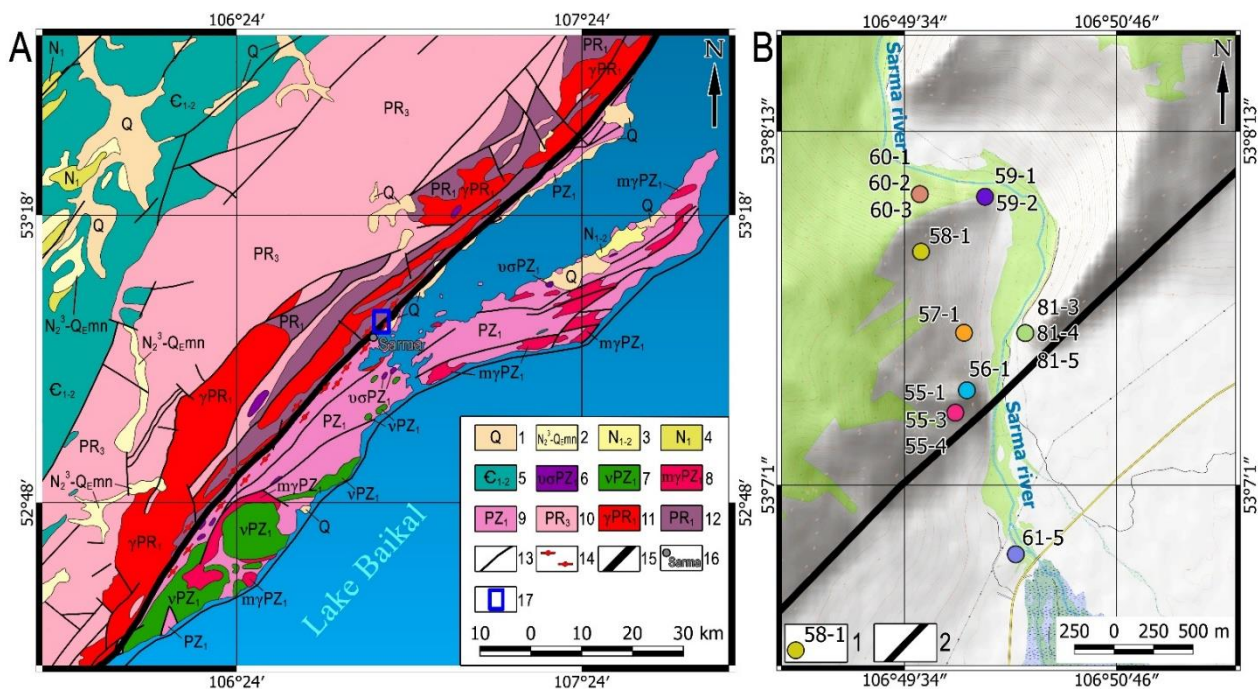


**Figure 2.** (A) Geological map of the Primorsky Fault [74,75,81–84]: 1—beach lacustrine deposits of Lake Baikal and alluvium of river valley terraces; 2—Manzurka Fm. alluvium; 3—Golumets Fm. alluvium; 4—Bayanday Fm. alluvium; 5—Lower and Middle Cambrian sediments on the Siberian craton; 6—Atarkhan peridotite–gabbro complex; 7—Ozersk gabbro–diorite complex; 8—Olkhon migmatite–granite complex; 9—Early Paleozoic metamorphic complexes of the Olkhon terrane; 10—Upper Proterozoic sediments (Baikal Group); 11—Primorsky granite complex; 12—Early Proterozoic craton basement; 13—main faults; 14—blastomylonite from the marginal suture of the Siberian craton; 15—Primorsky Fault; 16—Sarma village; 17—area of study. (B) Scheme of the oriented rock samples selection within the Primorsky Fault zone near Sarma village: 1—sampling points and their numbers; 2—Primorsky Fault.

The Primorsky deep fault has been well studied via geological, structural and tectono-physical methods [85]. The internal structure and dimensions of the zone of influence of this discontinuity have been studied carefully [73–75]. Due to its geomorphological severity, excellent exposure and accessibility for study, it is a reference point for paleotectonic reconstructions. Previously, it was established that, at the neotectonic stage, the main interface of the discontinuity was formed as a normal fault with an insignificant strike-slip component. It has been established that the Primorsky Fault had formed under conditions of crustal extension, as evidenced by the corresponding structural fault pattern. During Cenozoic rifting, the main displacement of the Primorsky Fault became active as a normal fault with a very insignificant sinistral strike-slip component [73]. By now, horizons of the Earth's

crust within the zone of the Primorsky Fault, which were previously located at seismic focal depths, have become accessible for visual geological study at the Earth's surface [86].

## 2.2. Collection of Rock Samples and Petrographic Analysis

An obligatory condition for the implementation of any microstructural analysis technique is the collection of spatially oriented samples, for which spatial fixation must be strictly observed throughout the entire duration of their processing [13,22,24–31]. Samples for petrographic and STMA studies were collected mainly in the outfall parts of the Sarma river. Rocky outcrops contain dislocated series of rocks of the Neo-Proterozoic that had undergone multistage physical and chemical transformations while being exposed to stress metamorphism. It is specific for amphibolite and greenschale facies of regional metamorphism.

The collected and analyzed samples of rocks are represented by numerous varieties of predominantly metamorphic and igneous rocks, as well as their metasomatically altered varieties. Shales (55-1, 55-3, 56-1, 57-1, 60-3, 81-3, 81-4, 81-5), gneissose granite (58-1, 59-1, 59-2, 60-1), plagiogranites (55-3, 55-4), amphibolites (60-2) and gabbro (61-5), varied in mineral composition, were distinguished (Table 1). The studied rock samples are classified as mylonites (81-4), blastomylonites (55-1, 55-3, 81-3, 81-5), cataclasites (55-4, 60-2, 60-3), blastocataclasites (56-1, 57-1, 61-5) and host rocks (58-1, 59-1, 59-2, 60-1), which were not subjected to intensive deformations. Among other characteristics, the type of deformation (brittle or ductile) was assessed, and metamorphic and metasomatic changes were marked.

**Table 1.** Petrographic description of rock samples.

Sample Number	Petrographic Type	Tectonite Type	Deformation Mode	Main Minerals * and Proportions (%)	Metamorphic and Metasomatic Transformations
55-1	Quartz-Sericite-Chlorite shale	Blastomylonite	Brittle	Q(60), Fsp(20), Src(10), Cl(5)	Complete recrystallization of quartz; sericite is formed by plagioclase; actinolite is chloritized
55-3	Contact rock: Quartz-Actinolite-Chlorite shale–Plagiogranite	Blastomylonite	Brittle and ductile	Fsp(60), Q(30), Cl(5), Ac(3)	Partial recrystallization of quartz; sericite is formed by plagioclase; actinolite is chloritized
55-4	Plagiogranite	Mylonite	Brittle	Q(60), Fsp(30), Ac(5), Cl(3), Src(2)	Partial recrystallization of quartz; sericite is formed by plagioclase
56-1	Plagioamphibolite shale	Mylonite	Brittle	Q(50), Fsp(40), Src(5), Cl(3), Ac(2)	Partial recrystallization of quartz; sericite is formed by plagioclase; actinolite is chloritized
57-1	Chlorite-Sericite-Plagioquartzite shale	Blastocataclasite	Brittle	Q(50), Fsp(30), Src(15), Cl(5), Ac(<1)	Partial recrystallization of quartz; sericite is formed by plagioclase; actinolite is chloritized
58-1	Leucocratic gneissose granite	Host rock	Brittle	Q(55), Fsp(35), Mu(2), Bt(2) Am(1)	Quartz is slightly granular
59-1	Leucocratic gneissose granite	Host rock	Brittle	Q(50), Fsp(35), Mu(5), Bt(4) Am(1)	Quartz is slightly granular
59-2	Leucocratic gneissose granite	Host rock	Brittle	Q(50), Fsp(35), Mu(7), Bt(5) Am(3)	Quartz is slightly granulated; about 10% potassium feldspar saussuritized

Table 1. Cont.

Sample Number	Petrographic Type	Tectonite Type	Deformation Mode	Main Minerals * and Proportions (%)	Metamorphic and Metasomatic Transformations
60-1	Gneissose granite	Host rock	Brittle	Q(55), Fsp(30), Bt(10)	Saussurite developed according to potassium feldspar; quartz is slightly granulated
60-2	Amphibolite	Cataclasite	Ductile	Am(55), Ep(25), Q(15), Fsp(5)	Recrystallization of quartz by schistosity
60-3	Amphibolite shale	Cataclasite	Ductile	Bt(50), Am(40), Q(5), Fsp(5)	Recrystallization of quartz by schistosity; amphibole is replaced by biotite
61-5	Gabbro	Blastocataclasite	Brittle	Am(35), Fsp(30), Px(25), Bt(5), Q(5)	Amphibole is substituted with biotite; quartz is recrystallized and switched into the matrix
81-3	Epidote shale	Blastomylonite	Brittle and ductile	Ep(60), Cl(30), Q(5),	Zone of stress metamorphism; a matrix of ground material of hydromicas formed over amphiboles; quartz is granulated
81-4	Amphibolite shale	Mylonite	Brittle and ductile	Cl(40), Fsp(20), Am(10), Ep(20), Q(10)	Zone of stress metamorphism; amphibole is replaced by chlorite and stretched into ribbons; Matrix-ground materials of potassium feldspar, chlorite, iron hydroxide
81-5	Epidote shale	Blastomylonite	Brittle and ductile	Ep(35), Q(15), Cl(40), Ca(10)	Zone of stress metamorphism; a matrix of ground material of hydromicas formed over amphiboles; quartz is granulated

\* Main minerals: Q—Quartz; Fsp—Potassium feldspar; Am—Amphibole; Px—Pyroxene; Ep—Epidote; Cl—Chlorite; Ac—Actinolite; Src—Sericite; Bt—Biotite; Mu—Muscovite; Ca—Calcite.

### 2.3. Fotos of Thin Sections

Images of oriented thin sections for microstructural mapping were obtained using an Olympus BX-51 optical microscope with an Olympus Camedia C7070zoom digital camera. To determine the orientation of microfractures in a GIS project and to calculate their geometric parameters (strike azimuth, length and aperture), all studied thin sections must be strictly oriented in space. This requirement must also be taken into account when taking photographs of individual parts of an oriented thin section. Separate parts of oriented thin sections were photographed in such a manner that a panoramic image of the entire section could be automatically constructed for them. Images of thin sections should have a resolution sufficient for analysis, which corresponds to at least 10,000 pixels along the smallest side. Photomosaics collected from separate sections should be provided with a scale ruler. Images were saved in TIFF format. Figure 3 shows thumbnail images of the studied thin sections.

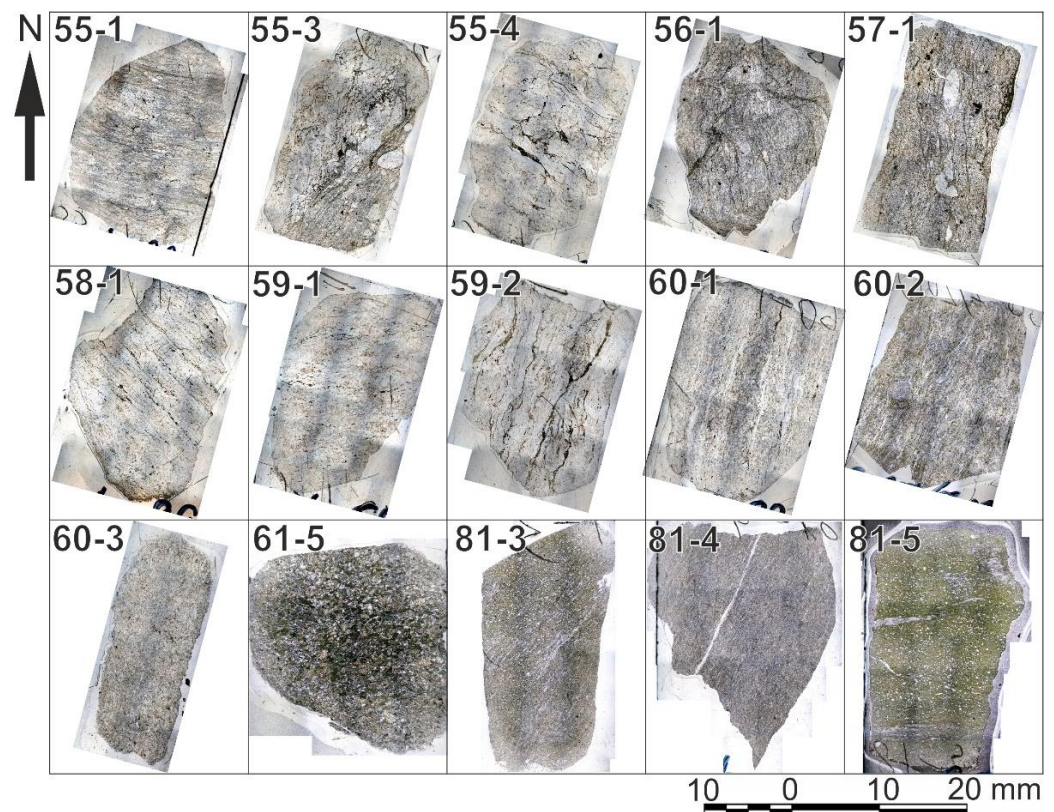


**Figure 3.** Images of the studied oriented thin sections obtained using the Olympus BX-51 optical microscope with the Olympus Camedia C7070zoom digital camera.

#### 2.4. Special Technique of Microstructural Analysis (STMA)

Given that the focus of the research is studying microfractures, the software used in STMA should implement and automate the following basic operations:

- Implementation of binding the rasters (images) of individual parts of a thin section, as well as their filling and docking in a single coordinate system;
- Determination of relative coordinates X and Y of any point in a thin section;
- Marking all microstructures within the thin section;
- Automatic determination and measurement of geometrical parameters of microstructures (strike azimuth, length and aperture);
- Identification of various ensembles and microstructure generations depending on the values of azimuth and their separate marking;
- Possibility of marking objects over type (microcracks filled with secondary fluid inclusions (FIPs), open or partially mineralized microcracks and microcracks filled with ore material);
- Calculation of porosity and permeability in paleo and modern conditions at various stages of deformation of geological bodies;
- Determination of quantitative and percent ratios of different types of microstructures and presentation of the results in the form of diagrams (graphs, rose-diagrams and histograms).

##### 2.4.1. Automatic Mapping of Microfractures

At the first stage of STMA, images of thin sections were mapped in a local rectangular coordinate system using QGIS (a free and open-source cross-platform GIS application). The global Mercator projection of Google Maps (EPSG-900913) [87] was used to display the image of the thin section.

At the second stage, a directional filtering of the image was carried out to remove the noise from sections located within a certain area of the image but without blurring its

edges. For this purpose, the Sobel operator was used. It is a discrete differential operator that calculates the approximate value of the image brightness gradient. The result of applying the Sobel operator at each point of the image is the vector of brightness gradient at that point.

The directional filters induce an optical effect of shadow at the image, as if it was illuminated by an oblique light. Directional filters are applied to the image using a convolution process by means of constructing a window, as a rule a (3 × 3) pixels box (Table 2) of Sobel kernel filters (Table 3). Sobel kernels generate an effective and faster method for evaluating lineaments (linear objects) in four principal directions [88–91].

**Table 2.** Floating image matrix, size 3 × 3.

Z1	Z2	Z3
Z4	Z5	Z6
Z7	Z8	Z9

**Table 3.** Sobel operator masks for four principal directions of filtration.

N-S (0°)			NE-SW (45°)			E-W (90°)			NW-SE (135°)		
−1	0	1	−2	−1	0	−1	−2	−1	0	1	2
−2	0	2	−1	0	1	0	0	0	−1	0	1
−1	0	1	0	1	2	1	2	1	−2	−1	0

The Sobel operator for horizontal and vertical brightness differences is defined by the following functions.

$$G_x = (Z7 + 2 \times Z8 + Z9) - (Z1 + 2 \times Z2 + Z3) \tag{1}$$

$$G_y = (Z3 + 2 \times Z6 + Z9) - (Z1 + 2 \times Z4 + Z7) \tag{2}$$

Based on these data, it is possible to calculate the value of the brightness difference.

$$G = \sqrt{(G_x^2 + G_y^2)} \tag{3}$$

The directional filtering operation narrows the boundary that exists between the values of neighboring pixels. In this study, directional filtering is used to improve the boundaries of gradient transition between pixel values in order to highlight certain characteristics of the image resting on their spatial frequency associated with textural features [92]. The original image of the section consists of three spectral channels: R, G and B. The R channel must be fed to the filter input, since the data obtained in red and infrared spectral ranges are more sensitive to structural features. Four filtered images were produced by ENVI software related to the directions N-S, NE-SW, E-W and NW-SE (Figure 4).

At the third stage, the automatic extraction of lineaments is carried out. At this stage, the first step is the edge detection procedure, which provides information about areas of sharp changes in the intensity of neighboring pixels by applying the Canny edge detector, and the second step is the detection of lineaments [93]. These steps can be performed using the “LINE” module of the PCI Geomatica software, which is a widely used module for automatic extraction of lineaments [93]. There are two categories of parameters in this module: the first category controls the edge detection step, the second one detects and extracts curves (Table 4).

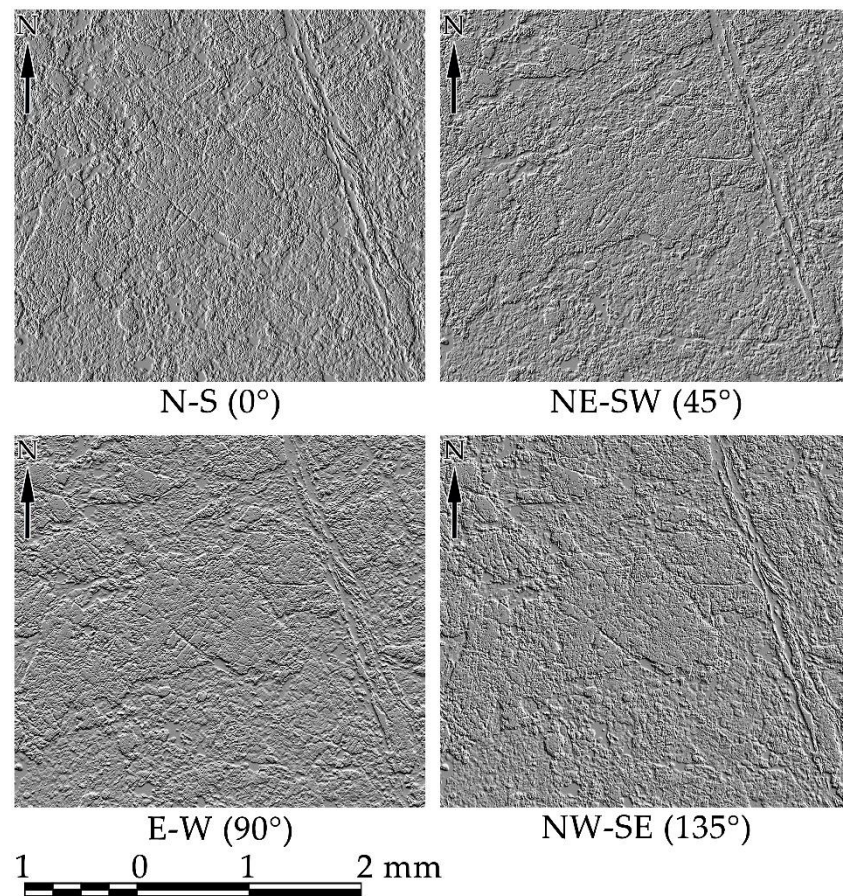


**Figure 4.** The result of filtering a part of the image of an oriented thin section with the Sobel operator in four principal directions.

**Table 4.** Parameters used for the PCI Geomatica LINE module.

Parameter	Description	Range and Unit
Edge Detection		
RADI	Filter radius. It specifies the radius of the edge detection filter (Filter de Canny).	0–8192 (pixel)
GTHR	Gradient threshold. It specifies the threshold for the minimum gradient level for an edge pixel to obtain a binary image (Filter de Canny).	0–255
Curve extraction		
LTHR	Length threshold: It specifies the minimum length of curve to be considered as lineament	0–8192 (pixel)
FTHR	Line fitting error threshold: It specifies the maximum error (in pixels) allowed in fitting a polyline to a pixel curve.	0–8192 (pixel)
ATHR	Angular difference threshold: It is the maximum angle between two vectors for them to be linked.	0–90 (degrees)
DTHR	Linking distance threshold: It specifies the minimum distance between the end points of two vectors for them to be linked.	0–8192 (pixel)

A number of experimental tests was performed using various combinations of values for each parameter of the LINE module to make an automatic selection of lineaments (microfractures) directly related to the structural and texture features in thin section images.

Parameters of the LINE module were verified visually. Default and calculated values of parameters of the LINE module are presented in Table 5.

**Table 5.** Default and verified values of the PCI Geomatica LINE module parameters for microfracture extraction.

Thresholds and Units	Default Value	Verified Value
RADI (pixels)	10	10
GTHR	100	35
LTHR (pixels)	30	60
FTHR (pixels)	3	5
ATHR (degrees)	30	45
DTHR (pixels)	20	20

Operating the program gives results that highlight linear objects, marking microfractures (Figure 5).

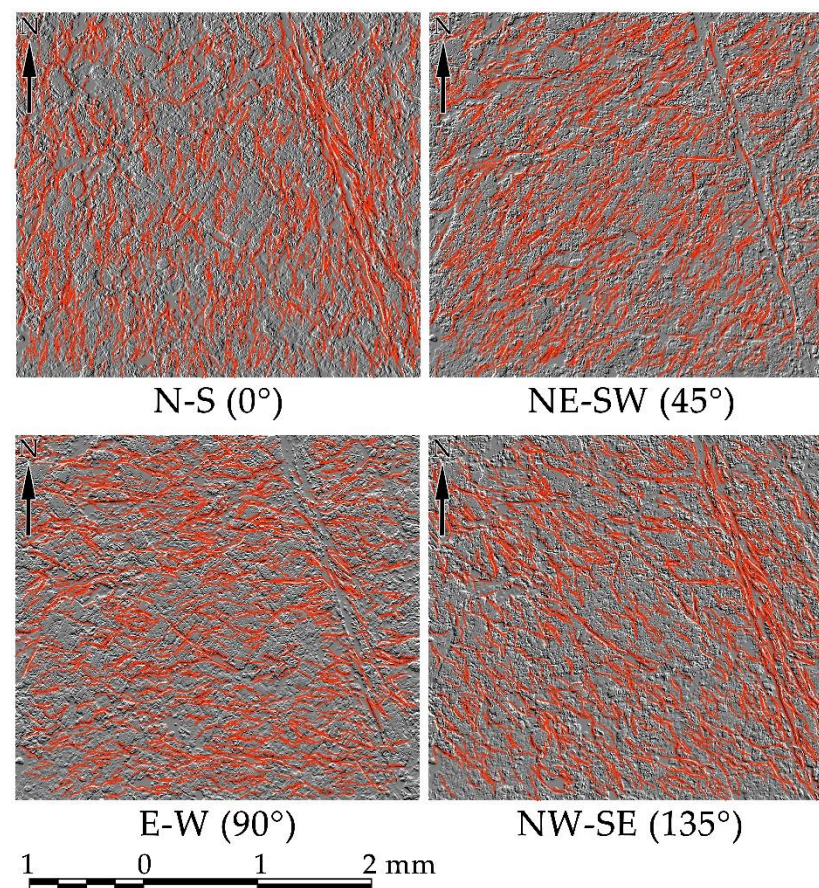


**Figure 5.** The result of detecting microfractures (red lines) by the LINE module in the PCI Geomatica according to the verified parameters of the part of the filtered image of the oriented thin section in four principal directions.

Directional filtering and Canny edge detecting results in constructing 4 groups of linear objects. The general ensemble of lineaments, obtained by a simple addition of the 4 groups, can be interpreted as the ensemble of detected microfractures. Figure 6 shows the image of a thin section with highlighted microfractures.

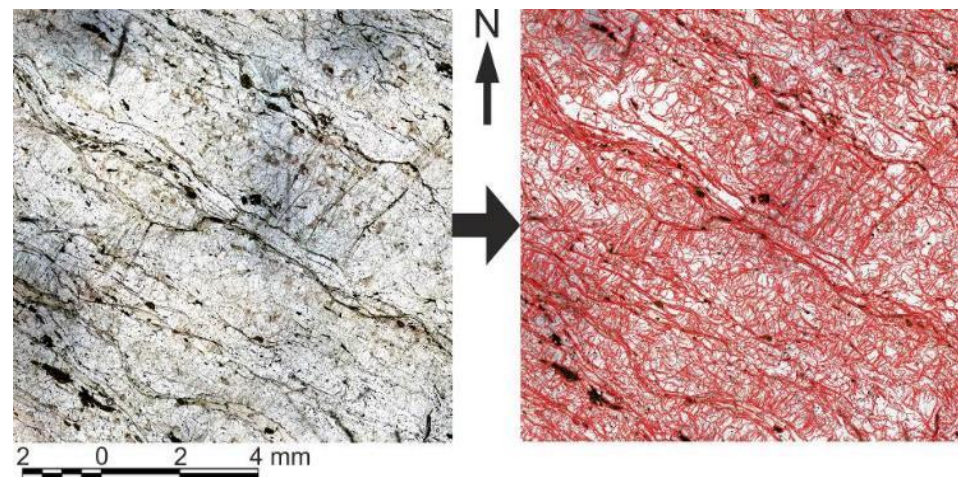


**Figure 6.** The result of detecting and marking microfractures in a part of the oriented thin section of the sample 58-1 using STMA.

#### 2.4.2. Microfracture Characteristics

The main quantitative parameters of the identified microfractures were calculated in QGIS using the Field Calculator tool [94]. The Field Calculator in the attribute table performs calculations based on existing attribute values or specific functions, such as calculating the length or the area of geometric objects. The results can be written to a new attribute column or used to update an existing column. The following parameters were automatically calculated for microfractures:

- Number of objects (microfractures);
- X and Y coordinates of the ends;
- Cumulative length;
- Length of each microfracture;
- Mean aperture of each microfracture;
- Length of each straight segment of each microfracture;
- Strike azimuth of each straight segment of each microfracture;
- Number of intersections of microfractures;
- Studied area of thin section, etc.

The spatial distribution of microfractures over the area of the section was analyzed by constructing density maps (P20) [95] using the Line Density tool. Rose diagrams of microfractures were built according to the values of their spatial orientation and taking into account their lengths. This allowed the visual assessment of the nature of distribution, the significance and severity of the selected linear objects in the thin section and to compare the intensity of deformations that resulted in the origination of a particular ensemble of microfractures at different stages of tectogenesis. Constructing rose diagrams has made it possible to carry out a comparative analysis of microfracture orientations and to identify different systems and generations of microfractures.

#### 2.4.3. Determination of Porosity and Permeability

Porosity and permeability of rocks were determined via the quantitative method proposed in [27,49]. The mapped microfractures were considered as a network of fractures. Cracks were approximated by disks. It was assumed that the maximum crack length corresponds to the disk diameter. In this study, the assumption was made that all the open microcracks that formed at a certain stage of deformation are interconnected. Thus, an equivalent crack with a total length of the disk diameter could be introduced. The effective porosity can be determined as follows:

$$\Phi = (L \cdot \pi \cdot e) / S \quad (4)$$

where  $L$  is the total length of a certain crack population,  $S$  is the area of the studied surface and  $e$  is the mean aperture of the crack ensemble [27,49].

The definition of fracture permeability is also based on the assumption that all fractures are connected and can be approximated by disks with an aperture equivalent to the fracture aperture. An assumption was introduced that cracks propagated perpendicularly to the plane of the oriented section and formed a non-uniform spatial distribution. This assumption allows to determine the microcrack permeability ( $K_f$ ) [27]:

$$K_f = (\varepsilon \cdot \pi \cdot N_f \cdot c^2 \cdot e^3) / 12 \quad (5)$$

where  $\varepsilon$  is the crack wall roughness coefficient,  $N_f$  is the volume density of crack population,  $c$  is the mean value of half-length of the cracks in the ensemble and  $e$  is the mean aperture of cracks.

If the surface density and half-length of all cracks are known, it is possible to determine their volumetric density [27,94]:

$$N_f = 2 / (S \cdot \pi \cdot c \cdot \sin\theta) \quad (6)$$

where  $\theta$  is the angle of crack incidence. If we assume that the cracks are perpendicular to the plane of the thin section, then  $\sin\theta = 1$ .

Thus, Formula (5) can be simplified as follows [27]:

$$K_f = (\varepsilon \cdot c \cdot e^3) / 6S \quad (7)$$

where  $K_f$  is the total or directive permeability (for a certain population of cracks), expressed in square meters ( $m^2$ ) or in darcy ( $1 \text{ darcy} = 0.987 \cdot 10^{-12} \text{ m}^2$ ).

It should be noted that the results of laboratory tests are in good correlation with the values of porosity and permeability calculated with this method [96–98].

### 3. Results

Using the STMA, quantitative parameters of microfractures in thin sections were calculated. The mean length of one object (microfracture segment) was about  $7.5 \mu\text{m}$ . The investigated area varied from 150 to  $370 \text{ mm}^2$ . Microstructural parameters are presented in Table 6 and in Figure 7. Samples 57-1 and 60-2 show maximum cumulative length and maximum number of microfractures (see Table 6 and Figure 7A,B). Minimal values of these parameters are observed in samples 55-3, 55-4, 81-4 and 81-5. The remaining samples are characterized by average values. The  $L/S$  ratios (see Table 6 and Figure 7C) reached maxima in samples 57-1, 60-2, 60-3, 61-5 and minima in samples 55-4, 81-3, 81-4, 81-5. Maximum values of the fracture intensity ( $F = N/L$ ) [99] were observed in samples 61-5, 81-3, 81-4, 81-5 and the minimum values—in samples 55-4, 60-2 (see Table 6 and Figure 7D). In general, the distribution of the fracture intensity is extremely nonuniform. Porosity and permeability can be most informative parameters for assessing the degree of deformations, since they are directly related to the physical properties of rocks. Porosity and permeability vary in a similar manner (see Table 6 and Figure 7E,F). Four clusters can be distinguished. The first cluster shows increased values of porosity and permeability. It includes samples 60-2, 60-3 and 61-5. The second cluster shows average values of porosity/permeability typical for samples 57-1, 58-1, 59-1 and 59-2. The third cluster includes only sample 60-1 and is associated with below-average values. Minimum values characterize the fourth cluster, which includes samples 55-1, 55-3, 55-4, 56-1, 81-3, 81-4 and 81-5. Figure 8 shows distributions of  $L/S$  and  $N/L$  versus permeability.

Table 6. Statistical parameters of microfractures.

Sample Number	Cumulative Length, mm (L)	Mean Aperture, Microns (e)	Number of Objects (N)	Studied Area, mm <sup>2</sup> (S)	Fracture Intensity F = N/L	L/S	Porosity, %	Permeability, m <sup>2</sup>
55-1	2416.76	3.1	326,112	282.52	0.0367	0.1156	1.13	1.44 × 10 <sup>-15</sup>
55-3	1349.20	2.7	177,193	151.99	0.0357	0.1200	1.02	9.84 × 10 <sup>-16</sup>
55-4	1168.48	3.3	142,813	287.83	0.0332	0.0549	0.57	8.22 × 10 <sup>-16</sup>
56-1	1849.79	2.6	251,385	243.86	0.0369	0.1025	0.84	7.52 × 10 <sup>-16</sup>
57-1	3579.96	4.5	484,590	337.23	0.0368	0.1435	2.03	5.45 × 10 <sup>-15</sup>
58-1	2233.05	4.8	292,253	251.44	0.0356	0.1200	1.81	5.53 × 10 <sup>-15</sup>
59-1	2801.10	4.9	379,502	306.55	0.0369	0.1235	1.90	6.05 × 10 <sup>-15</sup>
59-2	2387.49	4.8	309,648	251.95	0.0353	0.1281	1.93	5.90 × 10 <sup>-15</sup>
60-1	2881.68	3.9	384,124	354.89	0.0363	0.1098	1.34	2.71 × 10 <sup>-15</sup>
60-2	3444.97	5.4	424,009	326.80	0.0335	0.1425	2.42	9.35 × 10 <sup>-15</sup>
60-3	2648.34	5.6	356,331	242.95	0.0366	0.1473	2.59	1.08 × 10 <sup>-14</sup>
61-5	2501.05	5.3	346,100	259.61	0.0376	0.1302	2.17	8.08 × 10 <sup>-15</sup>
81-3	1958.90	2.9	278,241	325.88	0.0386	0.0812	0.74	8.26 × 10 <sup>-16</sup>
81-4	1241.22	3.2	173,286	276.85	0.0380	0.0606	0.61	8.27 × 10 <sup>-16</sup>
81-5	1173.13	3.1	166,625	371.26	0.0386	0.0427	0.42	5.30 × 10 <sup>-16</sup>

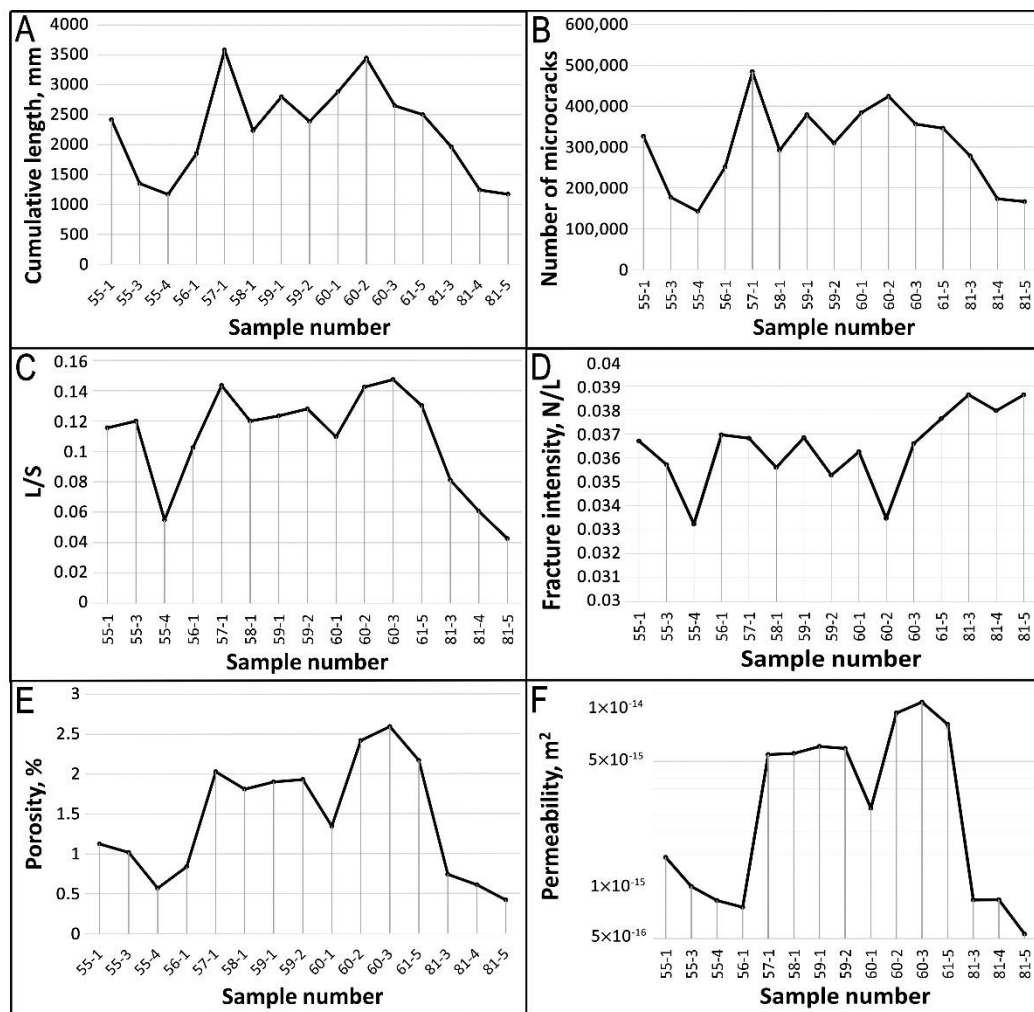


Figure 7. Graphs of the distribution of cumulative length (A), number of microfractures (B), L/S (C), Fracture intensity (D), porosity (E) and permeability (F) of microfractures in oriented thin sections.

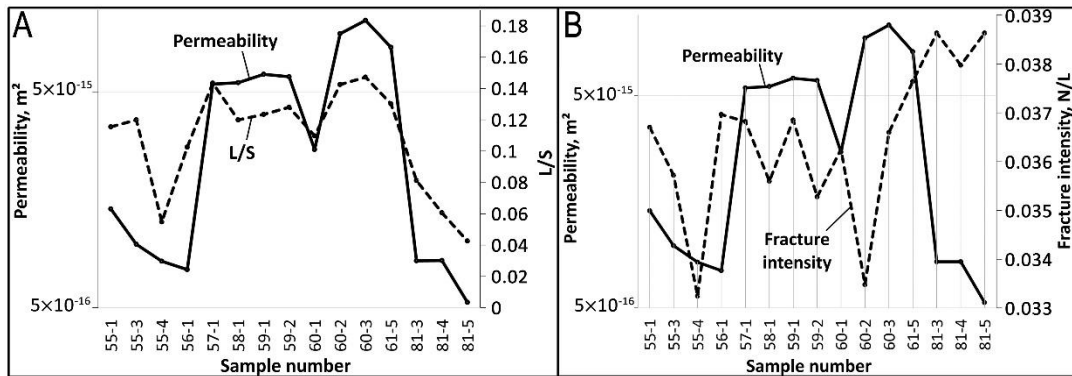


Figure 8. Graphs of the distribution of L/S (A) and N/L (B) versus permeability.

Fracture density maps (P20) [100] of the identified microfractures were built to assess the most permeable zones in the thin section. These maps show the areal distribution of microfractures (Figure 9).

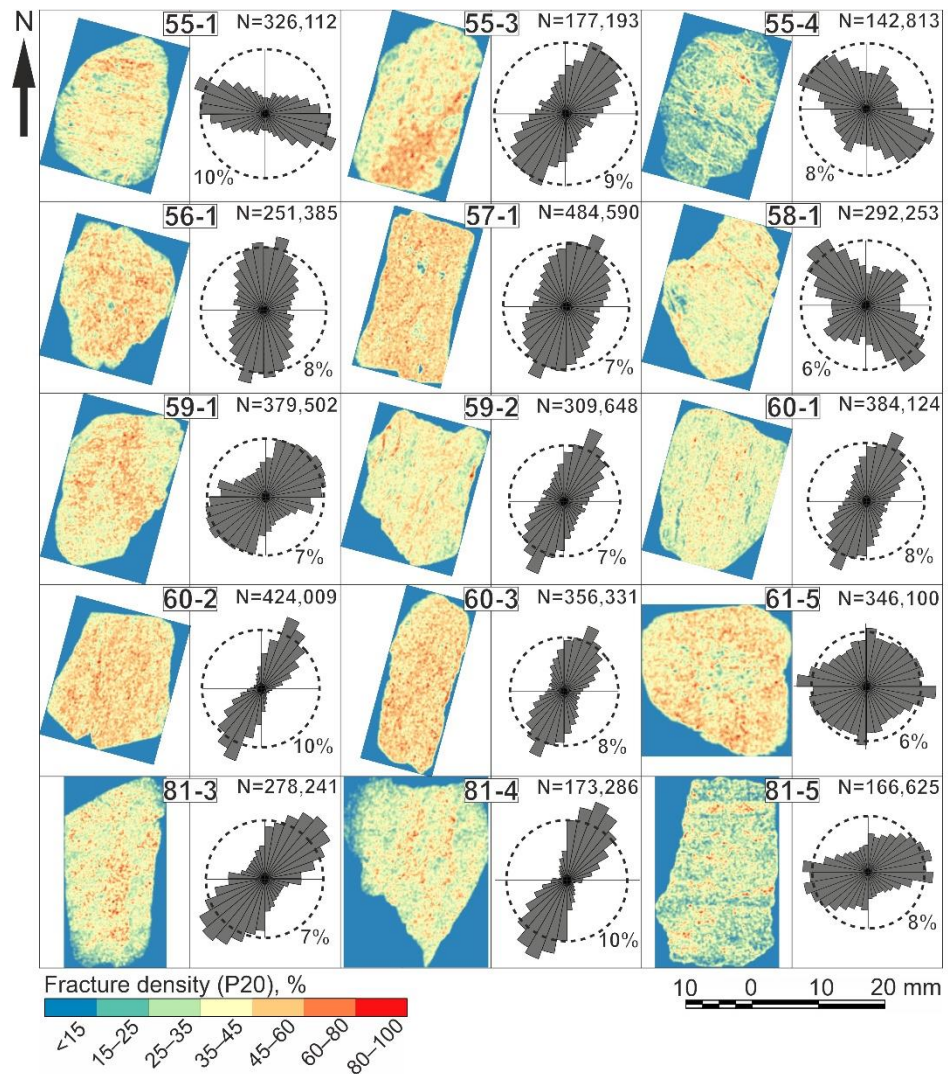
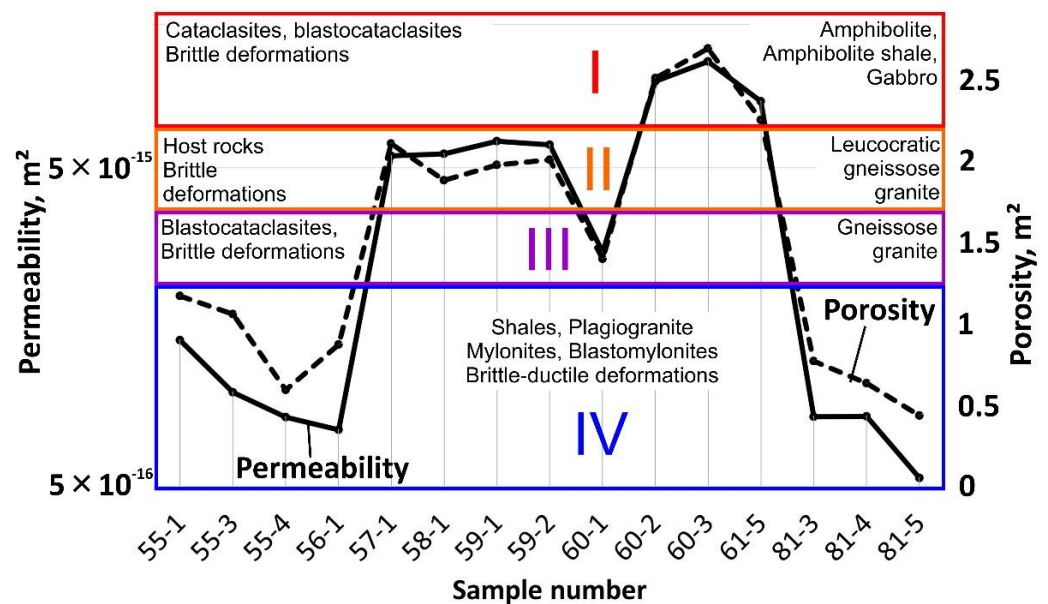


Figure 9. Fracture density (P20) maps and rose diagrams of microfractures in oriented thin sections.

Microfractures in the samples 56-1, 57-1, 59-1, 60-2, 60-3 and 61-5 have relatively uniform spatial distributions. In other thin sections, the distribution of microfractures is extremely uneven. Most often, the areas of maximum density of microfractures are confined to linearly elongated zones oriented in a certain manner. In sample 55-3, the density diagram clearly shows the contact of two rocks, which strike northeast. The rocks differ in the density of microfractures. Figure 9 also shows rose diagrams microfracture orientation. The results of orientation measurements can be used to reconstruct stress–strain fields, as well as to indirectly assess the degree of deformations that resulted in the origination of microfracture ensembles. In this paper, only the predominant directions of strikes of microfracture ensembles are considered. For a more detailed analysis, it is necessary to rank microfractures over length and orientation intervals, as well as structural and genetic types in order to identify individual ensembles associated with certain stages of deformations and parameters of the acting stress–strain field [6–9]. Samples 55-3, 59-1, 59-2, 60-1, 60-2, 60-3, 81-3 and 81-4 have predominantly northeastern orientation of microfractures. In samples 55-1 and 81-5, the microfractures are developed along the latitude with slight deviations to the northwest and northeast, respectively. Predominant northwestern orientations were identified in thin sections 55-4 and 58-1; a less pronounced northeastern orientation is also distinguished here. Samples 56-1 and 57-1 show north–northeastern orientations of microfractures. In the sample 61-5, microfractures are oriented almost uniformly in all directions.

A comparison of petrographic analysis data to the results of STMA reveals a high correlation. Thus, it was possible to identify clusters that characterize the heterogeneity of the fault zone. Four clusters were identified (Figure 10).



**Figure 10.** Integration of the data of petrographic and microstructural analyses of rock samples collected across the Primorsky Fault.

Cluster I shows the highest permeability. It includes samples of amphibolites, amphibolite schists and gabbro, which, by the type of tectonite, belong to cataclasites and blastocataclasites. Predominantly brittle deformations manifest in this area.

Cluster II shows lower permeability, which corresponds to host rocks represented by leucocratic granite gneisses. Brittle deformations also prevail here.

Cluster III was identified via only a single gneissose granite sample. It shows less pronounced brittle deformations, and it is a blastocataclasite according to the type of tectonite. The identification of this cluster is in doubt.

Cluster IV is represented by shales of different mineral composition and, to a lesser extent, by transformed plagiogranites. Cluster IV characterizes the transition from brittle to ductile deformations; it mainly includes mylonites and blastomylonites. Moreover, this cluster coincides with the zone of stress metamorphism established via petrographic analysis.

In order to characterize the fault zone, it is important to understand the change in the main quantitative characteristics of microfractures with distance from the fault trace (Figure 11). The total length and number of microstructures naturally increase with distance from the fault trace (Figure 11A). At the same time, a local maximum is fixed in the interval of 400–500 m, which was established in one sample (57-1). The distributions of L/S ratios and fracture intensity (N/L) show heterogeneous distribution (Figure 11B). In the immediate vicinity of the fault trace, the L/S values are in the range of 0.043–0.120. At a distance of more than 400 m from the fault trace, the values vary from 0.110 to 0.150. The fracture intensity near the fault trace varies in a wide range—from 0.033 to 0.039. Then, the values decrease linearly again to 0.033 with distance. It should be noted that all values of the N/L parameter are generally in a very narrow range. The porosity and permeability show a similar trend (Figure 11C). They are characterized by the lowest values near the fault trace (up to 200 m) and increase with distance from 400 to 1100 m. The maxima are reached at a distance of more than 1200 m.

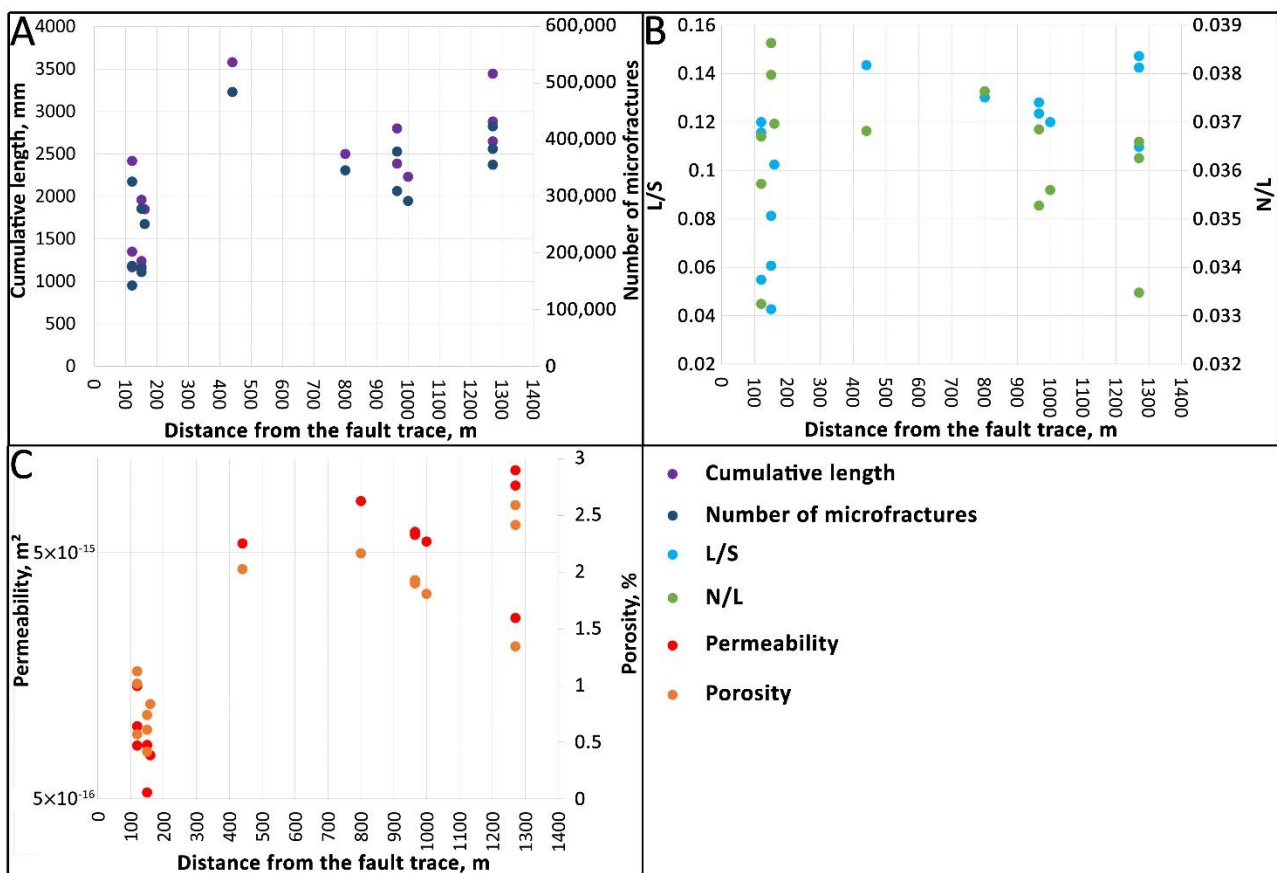


Figure 11. Graphs of the distribution of cumulative length versus number of microfractures (A), L/S versus N/L (B), permeability versus porosity (C) with distance from the fault trace.

#### 4. Discussion

The damage zone of the fault is usually characterized by a spatial heterogeneity of physical properties of rocks, types of their deformations and the development of secondary structures and microstructures [21,26]. At the same time, it is assumed that there is a certain zonality within this zone, the identification of which is one of the most important tasks of structural geology [6,18,21,24,33,69]. The solution of this problem is extremely difficult, since most fault structures are characterized by a long history of evolution and a successive change of several stages of deformations with certain parameters of the stress-strain field. The developed STMA method, using the GIS tools, significantly reduces the complexity of identifying and mapping microfractures in oriented thin sections, measuring and calculating their spatial and statistical parameters. The method provides necessary opportunities for a most comprehensive description and analysis of microfractures.

The Primorsky Fault is characterized by a long geological and tectonic history difficult for reconstruction. During its evolution it passed through numerous stages, including compression, strike-slip and tension [74,75,79,80]. The main challenge for a researcher is to restore the sequence of these stages. Microstructural analysis makes it possible to obtain additional information, which allows the identification of the stages of deformations and the reconstruction of the evolution of tectonic stress fields. At the same time, the STMA technique remains quite difficult to implement, and the process of sample preparation takes a long time. The first problem is the selection of a statistically significant number of oriented rock samples from outcrops. In the presented study, the main tasks were to confirm the efficiency of the developed approach and demonstrate its advantages. Therefore, the results of the analysis of 15 rock samples are preliminary. In the future, it is necessary to increase the density of rock sampling for a more comprehensive analysis of the heterogeneity of the fault zone, as well as to carry out selection along profiles across the fault strike throughout the entire damage zone.

In this study, fluid transfer properties are used as indicators of structural features of rock samples and probable heterogeneity of the fault zone. Porosity and permeability are in agreement with the results of petrographic analysis. It allows the identification of zones that characterize the heterogeneity of the fault. It is possible to create a preliminary scheme of heterogeneity of the fault (Figure 12). Three zones, which are characterized by different values of porosity and permeability, types of deformations and types of tectonites, were identified. The closest to the fault trace zone is characterized by the minimum values of porosity and permeability. Blastomylonites and mylonites formed there. The spatial distribution of parameters indicates intensive deformations within a zone 200 m thick. This zone can be considered as the fault core. During the formation of the network of microfractures, brittle and ductile deformations presumably took place. In the transition to the middle zone, an increase in porosity and permeability is observed. Rock samples mainly consist of cataclasites, and brittle deformations predominate. The farthest zone from the fault trace is characterized by the highest porosity and permeability; cataclasites and blastocataclasites are predominant there, and brittle deformations dominate. This model is consistent with most of the previously proposed models of fault zones [11,16–21,33,69].

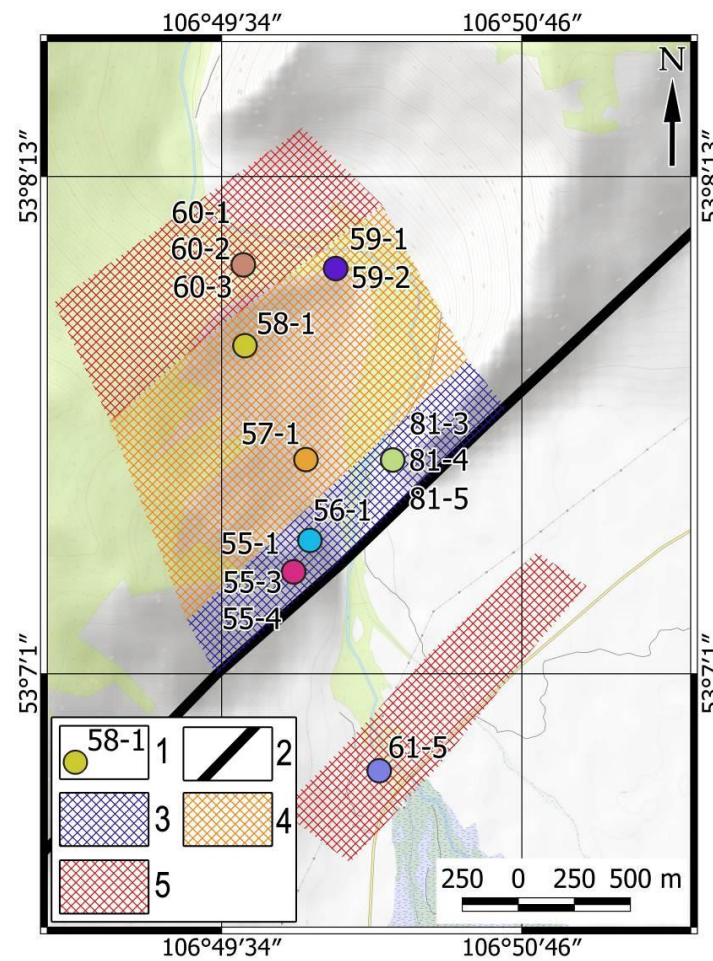


**Figure 12.** Scheme of heterogeneity of the Primorsky Fault zone based on microstructural analysis: 1—Sampling points and their numbers; 2—Primorsky Fault; 3—Cluster with low porosity and permeability, zone of blastomylonites and brittle and ductile deformations; 4—Cluster with medium porosity and permeability, zone of cataclasites and brittle deformations; 5—Cluster with high porosity and permeability, zone of cataclasites and blastocataclasites and brittle deformations.

Tectonophysical studies usually result in detecting variations of the parameters of the stress–strain field, which, in its turn, makes it possible to reconstruct the sequence of changes in deformations [3–12]. At the microscale, this issue can be resolved by studying fluid inclusion planes (FIPs) as tectonic indicators of changing stress–strain fields [23,27,48,49]. In studying the oriented sections of the collected samples, it was found that most of the microcracks are of mode I [34,47]. Resting on this fact, Figure 13A shows a preliminary scheme for interpreting the orientations of principal axes of stress fields. It should be noted that the identified orientations probably reflect the most pronounced stages of deformation. The preliminary interpretation of the position of stress axes for the sample 61-5 is ambiguous. Figure 13B shows the interpretation of the modern stress–strain field, identified by conducting an analysis of lineaments [75,101,102] in the area of the Sarma River. The orientation of the axes of modern stress field does not coincide with the orientation of the main axes of the stress fields identified in single samples. This suggests that main deformations observed in rock samples took place in previous geological epochs. It is worth mentioning that the presented results cannot be considered as final ones and a complete sequence of stress field changes can be reconstructed only based on a detailed study of cracks of various genetic types and an identification of their generations.

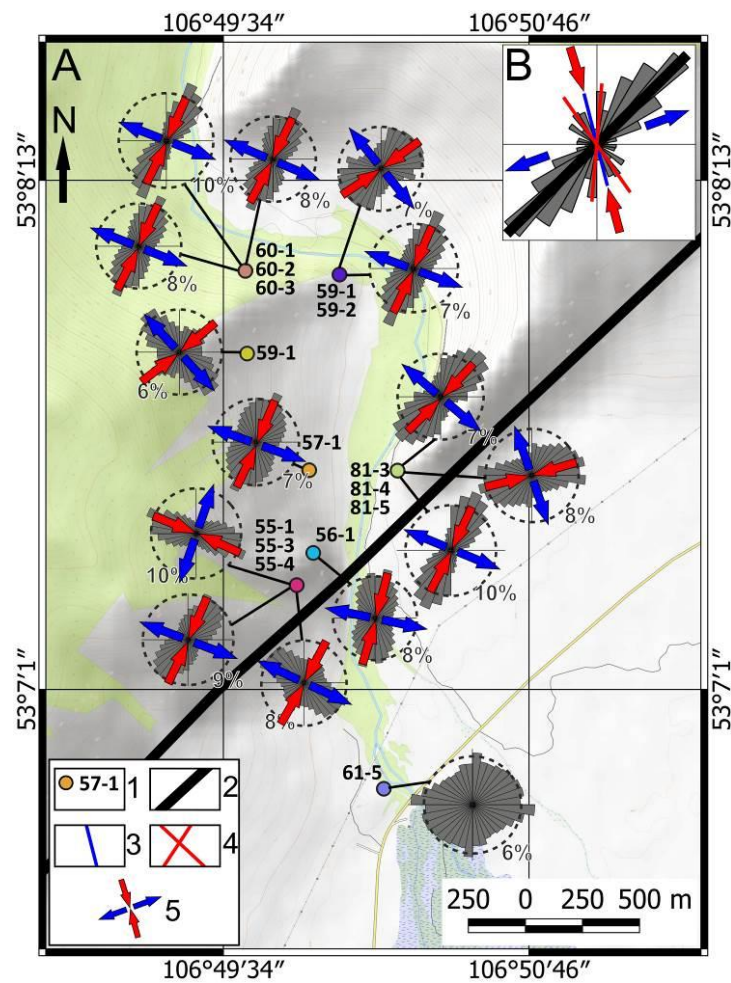


**Figure 13.** Scheme for interpreting the orientations of the principal axes of stress fields. (A) Interpretation of orientations of the main axes of the stress field performed for single rock samples based on the analysis of rose diagrams of microfractures, taking into account the fact that most studied microstructures are cracks of mode I; (B) interpretation of the orientations of principal axes of the modern stress field, performed via the analysis of lineaments in the area of the Sarma River [75,101,102]. 1—sampling points and their numbers; 2—Primorsky Fault; 3—cracks of mode I; 4—pair cracks of mode II; 5—orientation of the main axes of compression (red) and tension (blue).

## 5. Conclusions

A special technique of microstructural analysis (STMA) that utilizes advantages of GIS technologies is presented. Applying the GIS approach simplifies detection, vectorization and processing of large amounts of microstructural data (one thin section can contain up to  $10^5$  cracks). The GIS tools of STMA makes it possible to link all collected samples and their detected characteristics to maps of different types, as well as to simultaneously analyze microstructures and macrostructures identified via topographic and tectonic map data and satellite images. There is a unique possibility of linking and upscaling macro-, meso- and micro-characteristics of a rock massif, as well as restoring the sequence of changes in tectonic stress–strain fields at different scale levels and times of origination.

Applying the STMA algorithm, the structure of the damage zone of the Primorsky Fault was detected. Three permeable zones that are consistent with the results of petrographic studies have been identified. The thickness of the zone of most intensive deformations is estimated as 10–20 m.

**Author Contributions:** All authors contributed to the study conception and design. Conceptualization, S.U. and A.O.; methodology, S.U., A.S. and I.N.; software, I.N., A.U. and G.G.; validation, S.U., A.O., I.N. and A.S.; formal analysis, S.U., A.U. and A.G.; investigation, S.U., A.O. and A.G.; resources, S.U. and A.O.; data curation, G.G. and A.O.; writing—original draft preparation, S.U. and A.O.; visualization, S.U. and A.S.; supervision, S.U.; project administration, A.O.; funding acquisition, A.O. All authors have read and agreed to the published version of the manuscript.

**Funding:** This research was funded by the Russian Science Foundation, Grant No. 20-77-10087.

**Institutional Review Board Statement:** Not applicable.

**Informed Consent Statement:** Not applicable.

**Data Availability Statement:** All the data presented in this study are available from corresponding author on request.

**Acknowledgments:** Rock samples for analyses were delivered by IDG RAS in the frames of the Program No. FMWN-2022-0020 of the Ministry of Science and Higher Education of Russian Federation. The development of the special technique of microstructural analysis (STMA) was carried out by IGEM RAS in the frames of the Program of the Ministry of Science and Higher Education of Russian Federation.

**Conflicts of Interest:** The authors declare no conflict of interest.

## References

- Stephens, T.L.; Walker, R.J.; Healy, D.; Bubeck, A.; England, R.W. Mechanical models to estimate the paleostress state from igneous intrusions. *Solid Earth* **2018**, *9*, 847–858. [\[CrossRef\]](#)
- Yamaji, A.; Sato, K. Clustering of fracture orientations using a mixed Bing ham distribution and its application to paleostress analysis from dike or vein orientations. *J. Struct. Geol.* **2011**, *33*, 1148–1157. [\[CrossRef\]](#)
- De Guidi, G.; Caputo, R.; Scudero, S. Regional and local stress field orientation inferred from quantitative analyses of extension joints: Case study from southern Italy. *Tectonics* **2013**, *32*, 239–251. [\[CrossRef\]](#)
- Saintot, A.; Angelier, J. Tectonic paleostress fields and structural evolution of the NW-Caucasus fold-and-thrust belt from Late Cretaceous to Quaternary. *Tectonophysics* **2002**, *357*, 1–31. [\[CrossRef\]](#)
- Sim, L.A. Some methodological aspects of tectonic stress reconstruction based on geological indicators. *Comptes Rendus Geosci.* **2012**, *344*, 174–180. [\[CrossRef\]](#)
- Bott, M.H.P. The mechanics of oblique slip faulting. *Geol. Mag.* **1959**, *96*, 109–117. [\[CrossRef\]](#)
- Gushchenko, O.I. The method of kinematic analysis of destruction structures in reconstruction of tectonic stress fields. In *Fields of Stress and Strain in the Lithosphere*; Grigoriev, A.S., Osokina, D.N., Eds.; Nauka: Moscow, Russia, 1979; pp. 7–25. (In Russian)
- Rebetskii, Y.L.; Marinin, A.V. Stressed state of the Earth's crust in the western region of the Sunda subduction zone before the Sumatra-Andaman earthquake on December 26, 2004. *Dokl. Earth Sci.* **2006**, *407*, 321–325. [\[CrossRef\]](#)
- Gzovsky, M.V. *Fundamentals of Tectonophysics*; Nauka: Moscow, Russia, 1975; p. 536. (In Russian)
- Nikolaev, P.N. *Methodology of Tectonodynamic Analysis*; Nedra: Moscow, Russia, 1992; p. 295. (In Russian)
- Angelier, J. Fault slip analysis and paleostress reconstruction. In *Continental Deformation*; Hancock, P.L., Ed.; Pergamon Press: Oxford, UK, 1994; pp. 53–100.
- Lacombe, O. Do fault slip data inversions actually yield “paleostresses” that can be compared with contemporary stresses? A critical discussion. *Comptes Rendus Geosci.* **2012**, *344*, 159–173. [\[CrossRef\]](#)
- Heap, M.J.; Kushnir, A.R.L.; Gilg, H.A. Microstructural and petrophysical properties of the Permo-Triassic sandstones (Buntsandstein) from the Soultz-sous-Forêts geothermal site (France). *Geotherm. Energy* **2017**, *5*, 26. [\[CrossRef\]](#)
- Yang, G.; Leung, A.K.; Xu, N.; Zhang, K.; Gao, K. Three-dimensional physical and numerical modelling of fracturing and deformation behaviour of mining-induced rock slopes. *Appl. Sci.* **2019**, *9*, 1360. [\[CrossRef\]](#)
- Unver, B.; Yasitli, N. Modelling of strata movement with a special reference to caving mechanism in thick seam coal mining. *Int. J. Coal Geol.* **2016**, *66*, 227–252. [\[CrossRef\]](#)
- Petrov, V.A.; Poluektov, V.V.; Ustinov, S.A.; Minaev, V.A.; Lespinasse, M. Rescaling of fluid-conducting fault structures. *Dokl. Earth Sci.* **2017**, *472*, 130–133. [\[CrossRef\]](#)
- Petrov, V.A.; Poluektov, V.V.; Ustinov, S.A.; Minaev, V.A.; Lespinasse, M. Scale effect in a fluid-conducting fault network. *Geol. Ore Depos.* **2019**, *61*, 293–305. [\[CrossRef\]](#)
- Ben-Zion, Y.; Sammis, C.G. Characterization of fault zones. *Pure Appl. Geophys.* **2003**, *160*, 677–715. [\[CrossRef\]](#)
- Faulkner, D.R.; Lewis, A.C.; Rutter, E.H. On the internal structure and mechanics of large strike-slip fault zones: Field observations of the Carboneras fault in southeast Spain. *Tectonophysics* **2003**, *367*, 235–251. [\[CrossRef\]](#)
- Wibberley, C.A.J.; Shimamoto, T. Internal structure and permeability of major strike-slip fault zones: The Median Tectonic Line in Mie Prefecture, southwest Japan. *J. Struct. Geol.* **2003**, *25*, 59–78. [\[CrossRef\]](#)

21. Mitchell, T.M.; Faulkner, D.R. The nature and origin of off-fault damage surrounding strike-slip fault zones with a wide range of displacements: A field study from the Atacama fault system, northern Chile. *J. Struct. Geol.* **2009**, *31*, 802–816. [[CrossRef](#)]
22. Lespinasse, M.; Pecher, A. Microfracturing and regional stress field: A study of the preferred orientation of fluid-inclusion planes in a granite from the Massif Central, France. *J. Struct. Geol.* **1986**, *8*, 169–180. [[CrossRef](#)]
23. Boullier, A.-M. Fluid inclusions: Tectonic indicators. *J. Struct. Geol.* **1999**, *21*, 1229–1235. [[CrossRef](#)]
24. Wilson, J.E.; Chester, J.S.; Chester, F.M. Microfracture analysis of fault growth and wear processes, Punchbowl Fault, San Andreas system, California. *J. Struct. Geol.* **2003**, *25*, 1855–1873. [[CrossRef](#)]
25. Wise, D.U. Microjointing in basement, middle Rocky Mountains of Montana and Wyoming. *Geol. Soc. Am. Bull.* **1964**, *75*, 287–306. [[CrossRef](#)]
26. Hoxha, D.; Homand, F. Microstructural approach in damage modeling. *Mech. Mater.* **2000**, *32*, 377–387. [[CrossRef](#)]
27. Lespinasse, M.; Désindes, L.; Fratzek, P.; Petrov, V. Microfissural mapping of natural cracks in rocks: Implications for fluid transfers quantification in the crust. *Chem. Geol.* **2005**, *223*, 170–178. [[CrossRef](#)]
28. Duarte, M.T.; Liu, H.Y.; Kou, S.Q.; Lindqvist, P.A.; Miskovsky, K. Microstructural modeling approach applied to rock material. *J. Mater. Eng. Perform.* **2005**, *14*, 104–111. [[CrossRef](#)]
29. Lukin, L.I.; Chernyshev, V.F.; Kushnarev, I.P. *Microstructural Analysis*; Nauka: Moscow, Russia, 1965; p. 124. (In Russian)
30. Costin, L.S. A microcrack model for the deformation and failure of brittle rock. *J. Geophys. Res.* **1983**, *88*, 9485–9492. [[CrossRef](#)]
31. Kranz, R.L. Microcracks in rocks: A review. *Tectonophysics* **1983**, *100*, 449–480. [[CrossRef](#)]
32. Lawn, B. Fracture of brittle solids. In *Cambridge Solid State Science Series*, 2nd ed.; Cambridge University Press: Cambridge, UK, 1993; p. 378.
33. Brandes, C.; Tanner, D.C. Chapter 2—Fault mechanics and earthquakes. In *Understanding Faults*; Tanner, D., Brandes, C., Eds.; Elsevier: Amsterdam, The Netherlands, 2020; pp. 11–80. [[CrossRef](#)]
34. Jaeger, J.C.; Cook, N.G.W. *Fundamentals of Rock Mechanics*, 3rd ed.; Chapman and Hall: London, UK, 1979; p. 593.
35. Buck, W.R. The Dynamics of Continental Breakup and Extension. In *Treatise on Geophysics*, 2nd ed.; Schubert, G., Ed.; Elsevier: Amsterdam, The Netherlands, 2015; pp. 325–379. [[CrossRef](#)]
36. Tamanyu, S.; Fujimoto, K. On the models for the deep-seated geothermal system in the Kakkonda field. *Rept. Geol. Surv. Jpn.* **2000**, *284*, 133–164.
37. Fournier, R.O. Hydrothermal processes related to movement of fluid from plastic into brittle rock in the magmatic-epithermal environment. *Econ. Geol.* **1999**, *94*, 1193–1211. [[CrossRef](#)]
38. Harvey, P.K.; Brewer, T.S.; Pezard, P.A.; Petrov, V.A. *Petrophysical Properties of Crystalline Rocks*; The Geological Society: London, UK, 2005; p. 345.
39. Nelson, R.A. *Geological Analysis of Naturally Fractured Reservoirs*, 2nd ed.; Gulf Professional Publishing: Boston, MA, USA, 2001.
40. Snow, D.T. Anisotropic permeability of fractured media. *Water Resour. Res.* **1969**, *5*, 1273–1289. [[CrossRef](#)]
41. Moench, A.F. Double-porosity models for a fissured groundwater reservoir with fracture skin. *Water Resour. Res.* **1984**, *20*, 831–846. [[CrossRef](#)]
42. Ababou, R. *Approaches to Large Scale Unsaturated Flow in Heterogeneous Stratified and Fractured Geologic Media*; US Nuclear Regulatory Commission: Washington, DC, USA, 1991.
43. Long, J.C.S.; Gilmour, P.; Whitherspoon, P.A. A model for steady fluid flow in random three-dimensional networks of diskshaped fractures. *Water Resour. Res.* **1985**, *21*, 105–115. [[CrossRef](#)]
44. Gueguen, Y.; Dienes, J. Transport properties of rocks from statistics and percolation. *Math. Geol.* **1989**, *21*, 1–13. [[CrossRef](#)]
45. Canals, M.; Ayt Ougougdal, M. Percolation on anisotropic media, the Bethe lattice revisited. Application to fracture networks. *Nonlinear Processes Geophys.* **1997**, *4*, 11–18. [[CrossRef](#)]
46. Stauffer, D. *Introduction to Percolation Theory*; Taylor and Francis: London, UK, 1985; p. 124.
47. Homand, F.; Hoxha, D.; Belem, T.; Pons, M.N.; Hoteit, N. Geometric analysis of damaged microcracking in granites. *Mech. Mater.* **2000**, *32*, 361–376. [[CrossRef](#)]
48. Lespinasse, M.; Sausse, J. Quantification of fluid flow: Hydromechanical behaviour of different natural rough fractures. *J. Geochem. Explor.* **2000**, *69–70*, 483–486. [[CrossRef](#)]
49. Sausse, J.; Jacquot, E.; Fritz, B.; Leroy, J.; Lespinasse, M. Evolution of crack permeability during fluid-rock interaction. Example of the Brézouard granite (Vosges, France). *Tectonophysics* **2001**, *336*, 199–214. [[CrossRef](#)]
50. Sausse, J. Hydromechanical properties and alteration of natural fracture surfaces in the Soultz granite (Bas-Rhin, France). *Tectonophysics* **2002**, *348*, 169–185. [[CrossRef](#)]
51. Zhang, L.; Einstein, H.H. Estimating the intensity of rock discontinuities. *Int. J. Rock Mech. Min. Sci.* **2000**, *37*, 819–837. [[CrossRef](#)]
52. Zhang, L.; Einstein, H.H. Estimating the mean trace length of rock discontinuities. *Rock Mech. Rock Eng.* **1998**, *31*, 217–235. [[CrossRef](#)]
53. Riley, M.S. Fracture trace length and number distributions from fracture mapping. *J. Geophys. Res.* **2005**, *110*, B08414. [[CrossRef](#)]
54. Zeeb, C.; Gomez-Rivas, E.; Bons, P.D.; Blum, P. Evaluation of sampling methods for fracture network characterization using outcrops. *AAPG Bull.* **2013**, *97*, 1545–1566. [[CrossRef](#)]
55. Hirono, T.; Takahashi, M.; Nakashima, S. In situ visualization of fluid flow image within deformed rock by X-ray CT. *Eng. Geol.* **2003**, *70*, 37–46. [[CrossRef](#)]

56. Menendez, B.; David, D.; Martí'nez Nistal, A. Confocal scanning laser microscopy applied to the study of pore and crack networks in rocks. *Comput. Geosci.* **2001**, *27*, 1101–1109. [[CrossRef](#)]
57. Geraud, Y.; Caron, J.M.; Faure, P. Porosity network of a ductile shear zone. *J. Struct. Geol.* **1995**, *17*, 1757–1769. [[CrossRef](#)]
58. Passchier, C.W.; Trouw, R.A.J. *Microtectonics*, 2nd ed.; Springer: Berlin, Germany, 2005; p. 366.
59. Ustinov, S.; Petrov, V.; Poluektov, V.; Minaev, V. Calculation of filtration properties of the Antey uranium deposit rock massif at the deformation phases: Microstructural approach. In *Trigger Effects in Geosystems*; Kocharyan, G., Lyakhov, A., Eds.; Springer Nature: Cham, Switzerland, 2019; pp. 179–186.
60. Xu, J.; Zhao, X.; Liu, B. Digital image analysis of fluid inclusions. *Int. J. Rock Mech. Min. Sci.* **2007**, *44*, 942–947. [[CrossRef](#)]
61. Healy, D.; Rizzo, R.E.; Cornwell, D.G.; Farrell, N.J.C.; Watkins, H.; Timms, N.E.; Gomez-Rivas, E.; Smith, M. FracPaQ: A MATLAB™ toolbox for the quantification of fracture patterns. *J. Struct. Geol.* **2017**, *95*, 1–16. [[CrossRef](#)]
62. Zeeb, C.; Gomez-Rivas, E.; Bons, P.D.; Virgo, S.; Blum, P. Fracture network evaluation program (FraNEP): A software for analyzing 2D fracture trace-line maps. *Comput. Geosci.* **2013**, *60*, 11–22. [[CrossRef](#)]
63. Xu, C.; Dowd, P. A new computer code for discrete fracture network modelling. *Comput. Geosci.* **2010**, *36*, 292–301. [[CrossRef](#)]
64. Saha, K.; Frøyen, Y.K. *Learning GIS Using Open Source Software*, 1st ed.; Taylor and Francis Group: London, UK, 2021; p. 240. [[CrossRef](#)]
65. Longley, P.A.; Goodchild, M.F.; Maguire, D.J.; Rhind, D.W. *Geographic Information Systems and Science*, 2nd ed.; John Wiley and Sons: Chichester, UK, 2005.
66. Chang, K. *Introduction to Geographic Information System*, 4th ed.; McGraw-Hill Education: New York, NY, USA, 2016; p. 249.
67. Best, M.G. *Igneous and Metamorphic Petrology*, 2nd ed.; Blackwell Publishing Company: Oxford, UK, 2003; p. 752.
68. Letnikov, F.A.; Balyshv, S.O. *Petrophysics and Geoenergetics of Tectonites*; Nauka: Novosibirsk, Russia, 1991; p. 148. (In Russian)
69. Sherman, S.I. *Physics of Crustal Faulting*; Nauka: Novosibirsk, Russia, 1977; p. 102. (In Russian)
70. Mats, V.D. *The Cenozoic History and Structure of the Baikal Rift Basin*; GEO: Novosibirsk, Russia, 2001; p. 252. (In Russian)
71. Lunina, O.V.; Gladkov, A.S.; Cheremnykh, A.V. Fracturing in the Primorsky fault zone (Baikal Rift system). *Russ. Geol. Geophys.* **2002**, *43*, 446–455.
72. Mats, V.D.; Lobatskaya, R.M.; Khlystov, O.M. Evolution of faults in continental rifts: Morphotectonic evidence from the southwestern termination of the North Baikal basin. *Earth Sci. Front.* **2007**, *14*, 207–219. [[CrossRef](#)]
73. Cheremnykh, A.V. Stress fields in the Primorsky normal fault zone (Baikal rift). *Lithosfera* **2011**, *1*, 135–142.
74. Cheremnykh, A.V.; Cheremnykh, A.S.; Bobrov, A.A. Faults in the Baikal region: Morphostructural and structure-genetic features (case study of the Buguldeika fault junction). *Russ. Geol. Geophys.* **2018**, *59*, 1100–1108. [[CrossRef](#)]
75. Cheremnykh, A.V.; Burzunova, Y.P.; Dekabryov, I.K. Hierarchic features of stress field in the Baikal region: Case study of the Buguldeika Fault Junction. *J. Geodyn.* **2020**, *141–142*, 101797. [[CrossRef](#)]
76. Seminskii, K.Z.; Kozhevnikov, N.O.; Cheremnykh, A.V.; Pospeeva, E.V.; Bobrov, A.A.; Olenchenko, V.V.; Tugarina, M.A.; Potapov, V.V.; Burzunova, Y.P. Interblock zones of the northwestern Baikal rift: Results of geological and geophysical studies along the Bayandai Village—cape Krestovskii profile. *Russ. Geol. Geophys.* **2012**, *53*, 194–208. [[CrossRef](#)]
77. Lamakin, V.V. *Neotectonics of the Baikal Basin*; Nauka: Moscow, Russia, 1968; p. 247. (In Russian)
78. Aleksandrov, V.K. *Thrusts in the Baikal Region*; Nauka: Novosibirsk, Russia, 1990; p. 102. (In Russian)
79. Delvaux, D.; Moeys, R.; Stapel, G.; Melnikov, A.; Ermikov, V. Paleostress reconstructions and geodynamics of the Baikal region, Central Asia. Part I: Palaeozoic and Mesozoic pre-rift evolution. *Tectonophysics* **1995**, *252*, 61–101. [[CrossRef](#)]
80. Delvaux, D.; Moyes, R.; Stapel, G.; Petit, C.; Levi, K.; Miroshnitchenko, A.; Ruzhich, V.; San'kov, V. Paleostress reconstruction and geodynamics of the Baikal region, Central Asia. Part II: Cenozoic rifting. *Tectonophysics* **1997**, *282*, 1–38. [[CrossRef](#)]
81. Gladkochub, D.P.; Donskaya, T.V.; Wingate, M.T.D.; Poller, U.; Kr'oner, A.; Fedorovsky, V.S.; Mazukabzov, A.M.; Todt, W.; Pisarevsky, S.A. Petrology, geochronology, and tectonic implications of ca. 500 Ma metamorphic and igneous rocks along the northern margin of the Central-Asian Orogen (Olkhon terrane, Lake Baikal, Siberia). *J. Geol. Soc. Lond.* **2008**, *165*, 235–246. [[CrossRef](#)]
82. Gladkochub, D.P.; Donskaya, T.V.; Mazukabzov, A.M.; Sklyarov, E.V.; Fedorovskii, V.S.; Lavrenchuk, A.V.; Lepekhina, E.N. Fragment of the Early Paleozoic (~500 Ma) island arc in the structure of the Olkhon terrane, Central Asian fold belt. *Dokl. Earth Sci.* **2014**, *457*, 905–909. [[CrossRef](#)]
83. Donskaya, T.V.; Gladkochub, D.P.; Mazukabzov, A.M.; Fedorovsky, V.S.; Cho, M.; Cheong, W.; Kim, J. Synmetamorphic granitoids (~490 Ma) as accretion indicators in the evolution of the Olkhon terrane (Western Cisbaikalia). *Russ. Geol. Geophys.* **2013**, *54*, 1205–1218. [[CrossRef](#)]
84. Donskaya, T.V.; Gladkochub, D.P.; Fedorovsky, V.S.; Sklyarov, E.V.; Cho, M.; Sergeev, S.A.; Demonterova, E.I.; Mazukabzov, A.M.; Lepekhina, E.N.; Cheong, W.; et al. Pre-collisional (& 0.5 Ga) complexes of the Olkhon terrane (southern Siberia) as an echo of events in the Central Asian Orogenic Belt. *Gondwana Res.* **2017**, *42*, 243–263. [[CrossRef](#)]
85. Mats, V.D.; Perepelova, T.I. A new perspective on evolution of the Baikal Rift. *Geosci. Front.* **2011**, *2*, 349–365. [[CrossRef](#)]
86. Ruzhich, V.V.; Kocharyan, G.G.; Savelieva, V.B.; Travin, A.V. On the structure and formation of earthquake sources in the faults located in the subsurface and deep levels of the crust. Part II. Deep level. *Geodyn. Tectonophysics.* **2018**, *9*, 1039–1061. [[CrossRef](#)]
87. Lauf, G.B. The Transverse Mercator projection. *S. Afr. Geogr. J.* **2012**, *57*, 118–125. [[CrossRef](#)]
88. Suzen, M.L.; Toprak, V. Filtering of Satellite Images in Geological Lineament Analyses: An Application to a Fault Zone in Central Turkey. *Int. J. Remote Sens.* **1998**, *19*, 1101–1114. [[CrossRef](#)]

89. Gloaguen, R.; Marpu, P.R.; Niemeier, I. Automatic extraction of faults and fractal analysis from remote sensing data. *Nonlinear Process. Geophys.* **2007**, *14*, 131–138. [[CrossRef](#)]
90. Sedrette, S.; Rebai, N. Assessment Approach for the Automatic Lineaments Extraction Results Using Multisource Data and GIS Environment: Case Study in Nefza Region in North-West of Tunisia. In *Mapping and Spatial Analysis of Socio-Economic and Environmental Indicators for Sustainable Development. Advances in Science, Technology & Innovation (IEREK Interdisciplinary Series for Sustainable Development)*; Rebai, N., Mastere, M., Eds.; Springer: Berlin, Germany, 2019; pp. 63–69. [[CrossRef](#)]
91. Enoh, M.A.; Okeke, F.I.; Okeke, U.C. Automatic lineaments mapping and extraction in relationship to natural hydrocarbon seepage in Ugwueme, South-Eastern Nigeria. *Geod. Cartogr.* **2021**, *47*, 34–44. [[CrossRef](#)]
92. Paplinski, A. Directional filtering in edge detection. *IEEE Trans. Image Processing* **1998**, *7*, 611–615. [[CrossRef](#)]
93. Salui, C.L. Methodological validation for automated lineament extraction by LINE method in PCI Geomatica and MATLAB based Hough transformation. *J. Geol. Soc. India* **2018**, *92*, 321–328. [[CrossRef](#)]
94. QGIS User Guide—QGIS Documentation. Available online: [https://docs.qgis.org/3.16/en/docs/user\\_manual/index.html](https://docs.qgis.org/3.16/en/docs/user_manual/index.html) (accessed on 21 January 2022).
95. Underwood, E.E. *Quantitative Microscopy*; DeHoff, R.T., Rhines, F.N., Eds.; McGraw-Hill Book Co.: New York, NY, USA, 1968; p. 149.
96. Brace, W.F. Permeability of crystalline rocks: New in situ measurements. *J. Geophys. Res.* **1984**, *89*, 4327–4330. [[CrossRef](#)]
97. Gueguen, Y.; Shubnel, Y. Elastic wave velocities and permeability of cracked rocks. *Tectonophysics* **2003**, *370*, 163–176. [[CrossRef](#)]
98. Shmonov, V.M.; Vitovtova, V.M.; Zharikov, A.V. *Fluid permeability of Rocks of the Earth's Crust*; Scientific World: Moscow, Russia, 2002; p. 216. (In Russian)
99. Ortega, O.J.; Marrett, R.A.; Laubach, S.E. A scale-independent approach to fracture intensity and average spacing measurement. *AAPG Bull.* **2006**, *90*, 193–208. [[CrossRef](#)]
100. Bisdom, K.; Gauthier, B.D.M.; Bertotti, G.; Hardebol, N.J. Calibrating discrete fracture-network models with a carbonate three-dimensional outcrop fracture network: Implications for naturally fractured reservoir modeling. *AAPG Bull.* **2014**, *98*, 1351–1376. [[CrossRef](#)]
101. Rebetsky, Y.L.; Sim, L.A.; Marinin, A.V. *From Slickensides to Tectonic Stresses. Methods and Algorithms*; GEOS Publishing House: Moscow, Russia, 2017; p. 234. (In Russian)
102. Petrov, V.A.; Sim, L.A.; Nasimov, R.M.; Shchukin, S.I. Fault tectonics, neotectonic stresses, and hidden uranium mineralization in the area adjacent to the Strel'tsovka Caldera. *Geol. Ore Depos.* **2010**, *52*, 279–288. [[CrossRef](#)]